

V. Orlandini¹, R. Paciorri¹, A. Assonitis¹ & A. Bonfiglioli²

¹University of Rome "La Sapienza", Via Eudossiana 18, 00184 Rome, Italy ²Università degli Studi della Basilicata, Viale dell'Ateneo Lucano 10, 85100 Potenza, Italy

Abstract

This article proposes the use of inflatable ballutes to decelerate the first stage of a launcher during its reentry phase and to allow its recovery. In recent years, reusable launch vehicles (RLVs) have been proposed to significantly reduce the costs of space missions. The most famous case is the Falcon-9 first stage reused dozens of times. In this case the deceleration is producted by the propulsion system of the stage that is turned on during the re-entry. To evaluate the use of inflatable ballutes as an alternative braking systems, CFD simulations were performed using the conjugate heat transfer (CHT) technique. This technique allows to evaluate the drag and the heating caused by the high speed and by the exhaust gases of the propusion system. The results show that the use of the inflatable ballutes decelerates much more than the use of retropropulsion reducing the amount of the necessary propellant and can reduce the heating of the side wall of the reusable stage during the descent.

Keywords: Inflatable ballute, CFD, Re-entry trajectory, Conjugate heat transfer

1. Introduction

Since the 1950s, inflatable structures are studied for their ability to be compactly stored within a launch vehicle and then deployed in space. These structures are designed to supplant rigid counterparts that are bulkier and heavier.

The first inflatable space structures was the Echo satellites [1], a pair of spherical ballutes that acted as passive reflectors for microwave signals. In 1993, the Inflatable Torus Solar Array Technology (IT-SAT) [2] project was founded to create a solar array with inflatable booms. In 1996, the STS-77 space shuttle mission deployed the Inflatable Antenna Experiment (IAE) [3]. The antenna was inflated by the crew and maintained its shape for a complete orbit. In 1997 Mars Pathfinder used airbag system to land on the surface of Mars [4]. Inflatable structures are also considered for airlock or future habitat for space explorations. For this purpose a first experiment was made on the ISS in 2016 through Bigelow Expandable Activities Module (BEAM) [5]. The demonstration performed as expected and proved that inflatable habitats are feasible and applicable for future use. Finally, inflatable structures have also been designed to decelerate spacecraft during atmospheric re-entry. In November 2022, the LOFTID inflatable shield was successfully tested by NASA to replace rigid shields in future space missions [6]. Furthermore, these shields, which are called Hypersonic Inflatable Aerodynamic Decelerators (HIADs), could also be used for future aerocapture maneuvers [7] on other planets such as Mars, Venus and Uranus.

In this work we propose a new use of an inflatable ballute to decelerate the first re-entry stage of a launcher in order to reduce the propellant consumption caused by the use of retro-thrusters.

Reusable launch vehicles (RLVs) typically fall into three main categories: horizontal takeoff and landing [8]; vertical takeoff and horizontal landing [9]; and finally, vertical takeoff and vertical landing [10]. In recent years, the last option has gained significant importance, due to the development of the Falcon 9 [11]. The Falcon 9 uses the supersonic retropropulsion to maneuver the stage out of the

atmosphere and to decelerate during the re-entry phase. In particular, immediately after stage separation, the Falcon 9's first stage is rotated by 180 degrees to orient it in the right direction before the re-ignition of the engine. This is done by using cold gas thrusters located at the top of the booster. Afterward, the retropropulsion is used during the re-entry phase to decelerate the first stage. In the Falcon 9, this process has allowed the reuse of the launcher's first stage dozens of times, significantly reducing much the costs of space missions. Our goal instead is to replace the retro-propulsion to slow down the re-entry of the first stage and to reduce the heating during descent.

This paper is organized as follows: In Section 2, the test cases used for comparing retropropulsion and the use of inflatable ballutes are presented; Section 3 describes the governing equations for trajectory computing and for computing the aerothermal behaviour of the flow around the launcher and of its walls.; Section 4 outlines the numerical methods employed for solving the governing equations. In detail, numerical simulations are carried out using the CFD++ [12] software of METACOMP, that applies a conjugate heat transfer approach [13] (CHT) to couple the fluid-dynamic thermal field with the solid thermal one. Section 5 contains details on the domains and computational grids used for the different cases; Section 6 discusses and analyzes the results obtained; finally, Section 7 presents the conclusions and future developments.

2. Test-cases

2.1 Rocket with retro-propulsion

A small rocket, with the mission profile reported in Fig.1, was considered as test-case. After the engine starting the rocket lifts off, accelerates and increases its altitude. When the engine is turned off and the rocket continues its ascent in the coasting phase until the nose separates in the proximity of the apogee. Once the apogee is reached the stage rotates 180 degrees to orient itself in the right direction before the re-ignition of the engine. In the descent phase the retro-propulsion is actived during the supersonic flight to decelerate the rocket. Finally, rocket has a coasting phase until the landing.

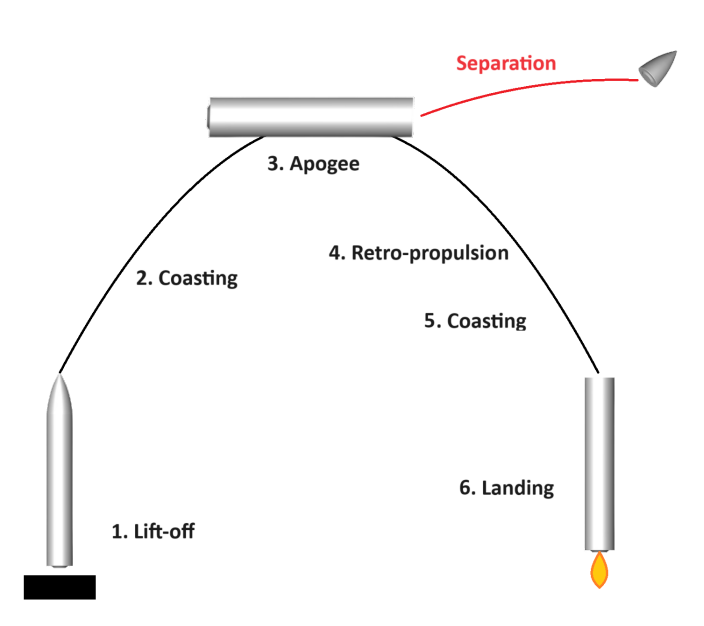


Figure 1 – Mission profile

Therefore there are two different geometrical configurations for the ascent phase and the descent phase shown in the Fig. 2. The diameter of this stage of the two cases is the same, equal to 1.5 meters while the length is different. For the ascent is equal to 11 meters while for the descent one is 8.62 meters. For this configuration we considered a launcher wall made of aluminum with the characteristics shown in the table 1. The initial mass of the launcher is considered constant in both cases and it is equal to 6000 kg.

The engine chosen for the rocket has the characteristics of the M10 developed by Avio [14]. The M10 is a liquid propellant engine fueled by liquid oxygen (LOX) and methane (LCH4) at a mixture ratio

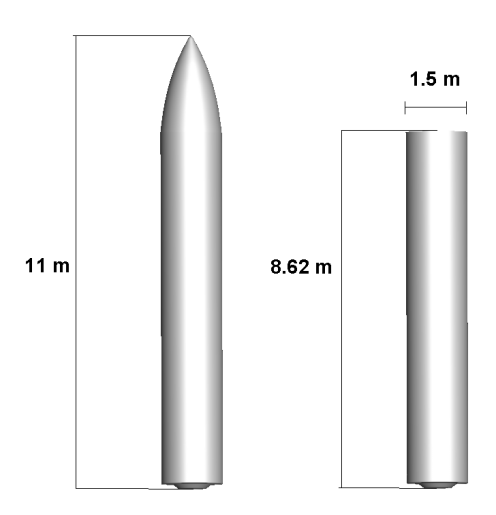


Figure 2 – Geometry of the rocket in ascent and descent phases

Material	Thickness	Density	Sp. Heat	Th. Cond.	Max allowable Temp.
	[mm]	[kg/m3]	[J/KgK]	[W/mK]	[K]
Aluminium	10	2700	897	237	573-623

Table 1 – Aluminium characterization

of 3.4 and based on a closed expansion thermodynamic cycle. It consists of a single combustion chamber regeneratively cooled and capable of multiple ignitions (up to 5). The M10 is capable of providing thrust up to 98 kN, with a required specific impulse of 362 s and it is also able to vary its thrust from 100% up to 75%. The flow conditions at the nozzle exit, with an expansion ratio of 10.923, was calculated using CEA [15] assuming two different total pressures in the combustion chamber for the thrust at 100% and 75%.

Thrust	P_0	P_e	T_e	γ_e	M_e	СО	CO_2	$\overline{H_2O}$
	[bar]	[Pa]	[K]					
100 %	52	55204	1578.17	1.2356	3.373	0.23386	0.25598	0.40165
75 %	40	42279	1554.35	1.2376	3.377	0.23563	0.25322	0.39912

Table 2 – Exit values from the nozzle

The exit flow conditions are reported in Tab.2 with P_e the exit pressure, T_e the exit temperature, γ_e the specific heat ratio of the mixture, M_e the exit Mach number and the gas concentrations at the exit section of the rocket nozzle.

2.2 Rocket with ballutes

In order to reduce the use of propellant in the descent phase we propose the use of an inflatable ballute whose the geometry is shown in Fig.3. The geometry consists in a toroid with a major radius of 1.314 meters and a minor radius of 0.25 meters and this structure are made of Kevlar [16] whose thermal characteristics are shown in Tab.3. The ballute is deployed at the beginning of the descent phase and remains open until landing. It is inflated to the maximum allowable inflation pressure which increases its structural rigidity and it is considered as a rigid body in fluid-dynamics modeling.

3. Governing equations

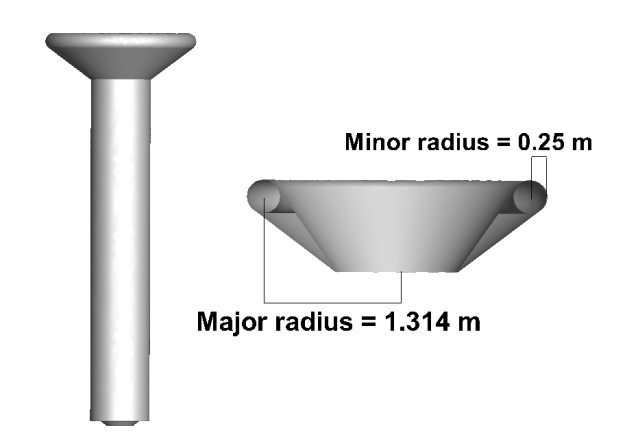


Figure 3 - Geometry of the ballute

Material	Thickness	Density	Sp. Heat	Th. Cond.	Max allowable Temp.	mass
	[mm]	[kg/m3]	[J/KgK]	[W/mK]	[K]	[kg]
Kevlar	1	1440	1400	0.04	422-450 K	56.75

Table 3 - Kevlar characterization

3.1 Trajectory-phase

The equations used to compute the trajectories are:

$$\dot{r} = V \sin \theta$$

$$\dot{\theta} = -\frac{1}{2}\rho V \left(\frac{C_L A}{m}\right) - g \frac{\cos \theta}{V} + \frac{V}{R_T + r} \cos \theta$$

$$\dot{V} = -\frac{1}{2}\rho V^2 \left(\frac{C_D A}{m}\right) - g \sin \theta + \frac{T}{m}$$
(1)

This is a system of three degrees of freedom where r represents the altitude, θ the flight path angle and V the velocity, g is the gravitational acceleration, R_T is the radius of the Earth, T is the thrust of the engine, m is the overall mass of the system and ρ represents the density that varies with the altitude. In particular, is computed using the Earth-GRAM model developed by NASA [17]. The term $\frac{C_LA}{m}$ is zero because the angle of attack is not considered in the simulation and no lift is generated during the ascent and descent phases. The term $\frac{C_DA}{m}$ is the reciprocal of the ballistic coefficient $\beta = \frac{m}{C_DA}$ and represents the most important parameter that regulates the trajectory. The ballistic coefficient varies over time if the engine is working due to propellant consumption and, furthermore, the value of the C_D i.e. the aerodynamic drag coefficient varies with the freestream conditions. While the mass variation can be easy estimated if the engine specifications are known, an accurate estimate of C_D requires CFD simulations of the different flow conditions occurring along the trajectory. Therefore, the CFD analysis was used to calculate the C_D and the heating of the side wall during the rocket flight. In particular, the C_D is computed by the relation:

$$C_D = \frac{2D}{\rho_{\infty} V_{\infty}^2 A} \tag{2}$$

where D is the aerodynamic drag force, ρ_{∞} the free-stream density, V_{∞} the freestream velocity that vary along the rocket trajectory and A the cross-section area of the rocket or of the ballute.

3.2 Fluid-phase

As said in the paragraph 2.1, the flow at the exit of the nozzle is a mixture of gases different from air. Therefore, in the fluid-phase we consider the governing equations for turbulent flows of multi-species mixture that in three-dimensional Cartesian coordinates can be written as:

$$\frac{\partial U}{\partial t} + \frac{\partial}{\partial x}(F_1 + G_1) + \frac{\partial}{\partial y}(F_2 + G_2) + \frac{\partial}{\partial z}(F_3 + G_3) = \dot{S}$$
(3)

where U is the conservation variable vector; F_1 , F_2 and F_3 are the inviscid flux vectors; G_1 , G_2 and G_3 are the viscous flux vectors; and S is the source term vector that is zero because no reactions are considered in these simulations. These are given as:

$$\mathbf{U} = \begin{pmatrix} e \\ \rho \\ \rho u \\ \rho v \\ \rho w \\ \rho \sigma_{1} \\ \vdots \\ \rho \sigma_{N-1} \end{pmatrix} \qquad \mathbf{F}_{1} = \begin{pmatrix} (e+p)u \\ \rho u \\ \rho u \\ \rho v u \\ \rho w u \\ \rho u \sigma_{1} \\ \vdots \\ \rho u \sigma_{N-1} \end{pmatrix} \qquad \mathbf{F}_{2} = \begin{pmatrix} (e+p)v \\ \rho v \\ \rho uv \\ \rho v v \\ \rho v v \\ \rho v \sigma_{1} \\ \vdots \\ \rho v \sigma_{N-1} \end{pmatrix} \qquad \mathbf{F}_{3} = \begin{pmatrix} (e+p)w \\ \rho w \\ \rho uw \\ \rho v w \\ \rho w \sigma_{1} \\ \vdots \\ \rho w \sigma_{N-1} \end{pmatrix} \qquad (4)$$

$$\mathbf{G_{1}} = \begin{pmatrix} \dot{q}_{x} - u\tau_{xx} - v\tau_{xy} - w\tau_{xz} \\ 0 \\ -\tau_{xx} \\ -\tau_{xy} \\ -\tau_{xz} \\ \rho D_{1,m} \frac{\partial \sigma_{1}}{\partial x} \\ \vdots \\ \rho D_{N-1,m} \frac{\partial \sigma_{N-1}}{\partial x} \end{pmatrix} \qquad \mathbf{G_{2}} = \begin{pmatrix} \dot{q}_{y} - u\tau_{yx} - v\tau_{yy} - w\tau_{yz} \\ 0 \\ -\tau_{yx} \\ -\tau_{yz} \\ \rho D_{1,m} \frac{\partial \sigma_{1}}{\partial y} \\ \vdots \\ \rho D_{N-1,m} \frac{\partial \sigma_{N-1}}{\partial z} \end{pmatrix} \qquad \mathbf{G_{3}} = \begin{pmatrix} \dot{q}_{z} - u\tau_{zx} - v\tau_{zy} - w\tau_{zz} \\ 0 \\ -\tau_{zx} \\ -\tau_{zy} \\ -\tau_{zz} \\ \rho D_{1,m} \frac{\partial \sigma_{1}}{\partial z} \\ \vdots \\ \rho D_{N-1,m} \frac{\partial \sigma_{N-1}}{\partial z} \end{pmatrix}$$

being e the total energy, ρ the density, p the pressure, u, v and w the velocity components in the x, y and z directions respectively and σ_i the mass fraction of species i. The species diffusion terms are modeled using the species gradients and the molecular diffusion coefficient of the i-th specie in the mixture, $D_{1,m}$, which is computed under the assumption that the Schmidt number is constant ($S_C = 0.7$). For a Newtonian fluid, the stresses and strains are linearly related:

$$\tau_{xx} = 2(\mu + \mu_t) \frac{\partial u}{\partial x} - \frac{2}{3}(\mu + \mu_t) \phi
\tau_{yy} = 2(\mu + \mu_t) \frac{\partial v}{\partial y} - \frac{2}{3}(\mu + \mu_t) \phi
\tau_{zz} = 2(\mu + \mu_t) \frac{\partial w}{\partial z} - \frac{2}{3}(\mu + \mu_t) \phi
\tau_{xy} = \tau_{yx} = (\mu + \mu_t) (\frac{\partial u}{\partial y} + \frac{\partial v}{\partial x})
\tau_{xz} = \tau_{zx} = (\mu + \mu_t) (\frac{\partial u}{\partial z} + \frac{\partial w}{\partial x})
\tau_{yz} = \tau_{zy} = (\mu + \mu_t) (\frac{\partial v}{\partial z} + \frac{\partial w}{\partial y})$$
(5)

where μ is the molecular viscosity of the mixture, μ_t is the turbulent viscosity and ϕ is the dilation given by:

$$\phi = \left(\frac{\partial u}{\partial x} + \frac{\partial v}{\partial y} + \frac{\partial w}{\partial z}\right) \tag{6}$$

From Fourier's law of conduction, we can write:

$$\dot{q}_{x} = -(k+k_{t})\frac{\partial T}{\partial x}$$

$$\dot{q}_{y} = -(k+k_{t})\frac{\partial T}{\partial y}$$

$$\dot{q}_{z} = -(k+k_{t})\frac{\partial T}{\partial z}$$
(7)

where k is the thermal conductivity of the mixture and k_t is the turbulent thermal conductivity. Molecular viscosity and thermal conductivity are obtained from Sutherland's law:

$$\frac{\mu}{\mu_{ref}} = \left(\frac{T}{T_{ref}}\right)^{1.5} \frac{T_{ref} + S_{\mu}}{T + S_{\mu}}$$

$$\frac{k}{k_{ref}} = \left(\frac{T}{T_{ref}}\right)^{1.5} \frac{T_{ref} + S_{k}}{T + S_{k}}$$
(8)

The turbulent thermal conductivity k_t is obtained from the turbulent Prandlt number (Pr_t)

$$k_t = \frac{\mu_t c_p}{Pr_t} \tag{9}$$

which is set to 0.9. The turbulent viscosity μ_t is calculated using the Spalart-Allmaras (SA) model [18].

$$\frac{\partial}{\partial x_j}(u_j\tilde{\mathbf{v}}) = c_{b1}f_{r1}(1 - f_{t2})\tilde{\mathbf{S}}\tilde{\mathbf{v}} + \frac{1}{\sigma}(\nabla \cdot ((\mathbf{v} + \tilde{\mathbf{v}})\nabla \tilde{\mathbf{v}}) + c_{b2}(\nabla \tilde{\mathbf{v}})^2) - \left(c_{w1}f_w - \frac{c_{b1}}{\kappa^2}f_{t2}\right)\left(\frac{\tilde{\mathbf{v}}}{d}\right)^2 + f_{t1}\Delta U^2.$$
 (10)

The SA equation provides a variable \tilde{v} and then the turbulent kinematic viscosity v_t is obtained from the variable \tilde{v} by means of

$$v_t = \tilde{v} f_{v1} \tag{11}$$

where f_{v1} , f_{t1} , f_{t2} , f_w , f_{t2} and f_{r1} are dumping functions, c_{b1} , c_{b2} and c_{w1} are constants and hence the turbulent viscosity be given by

$$\mu_t = \rho \, V_t \tag{12}$$

The constants and functions of the SA model are reported in Ref. [18].

Each component of the mixture satisfies the ideal gas equation using the Dalton's law, the mixture quantities can be written as

$$p = \rho \bar{R}T$$

$$\bar{R} = R_0 \sum_{i} \frac{\sigma_i}{W_i}$$

$$h = \sum_{i} \sigma_i \int_{-T}^{T} c_{p_i} dT + \sum_{i} \sigma_i \Delta H f_i$$

$$e = \frac{p}{\gamma - 1} + \rho \frac{u^2 + v^2}{2} + \sum_{i=1}^{N} \rho \sigma_i \Delta H f_i$$

$$\gamma = 1 + \frac{1}{\frac{\bar{C}_p}{R \sum_{i} (\sigma_i / W_i)} - 1}$$

$$\bar{c}_p = \frac{1}{T} \sum_{i} \sigma_i \int_{T} c_{p_i} dT$$

$$(13)$$

where c_{p_i} is the specific heat of i-th species, R_0 the universal gas constant, T the static temperature, $\Delta H f_i$ the enthalpy of formation of i-th species, ρ the density, σ_i the mass fraction of the i-th species and γ the ratio of specific heats for the mixture.

3.3 Solid phase

In this study, the wall is modeled as an isotropic homogeneous solid material having the same density, thermal conductivity and specific heat in every point. Inside the solid material there is only heat exchange by conduction, therefore the temperature field can be modeled by the Fourier equation:

$$\alpha \frac{\partial T}{\partial t} = k \nabla^2 T \tag{14}$$

To connect the thermal field of the solid wall with that of the flow-field, the equality of the thermal fluxes at the solid/fluid interface is imposed.

$$k_f \frac{\partial T}{\partial n} \bigg|_f = k_s \frac{\partial T}{\partial n} \bigg|_s \tag{15}$$

where k_f and k_s are the thermal conductivities of the solid phase and of the fluid phase and $\frac{\partial T}{\partial n}\Big|_s$ and $\frac{\partial T}{\partial n}\Big|_s$ are the temperature gradients calculated at the interface in the fluid phase and in the solid phase, respectively.

4. Numerical model

4.1 Numerical integration for the trajectory

The system of ordinary differential equations 1 can be rewritten in compact form as $\dot{y} = f(t,y)$. The fourth-order Runge-Kutta method was used to integrate this equation systems. This process involves calculating four intermediate values k_1 , k_2 , k_3 , and k_4 at each time interval and for each equation, for a total of twelve coefficients, which are then used to update the solution. Given the initial condition $y(t_0) = y_0$, the method proceeds as follows:

- 1. Calculate the increment Δt based on the desired step size.
- 2. Compute the four intermediate slopes k_1 , k_2 , k_3 , and k_4 as follows:

$$k_{1} = \Delta t f(t_{n}, y_{n})$$

$$k_{2} = \Delta t f(t_{n} + \frac{\Delta t}{2}, y_{n} + \frac{k_{1}}{2})$$

$$k_{3} = \Delta t f(t_{n} + \frac{\Delta t}{2}, y_{n} + \frac{k_{2}}{2})$$

$$k_{4} = \Delta t f(t_{n} + \Delta t, y_{n} + k_{3})$$
(16)

3. Compute the weighted average of these slopes to obtain the final approximation:

$$y_{n+1} = y_n + \frac{1}{6}(k_1 + 2k_2 + 2k_3 + k_4)$$
(17)

4. Repeat steps 1-3 until the desired endpoint is reached.

4.2 Numerical integration for the fluid-dynamic

Numerical simulations are performed using a second order accurate in time and space finite volume discretization [12]. In a finite volume method, the conservation equations in integral form both of the solid and fluid phase are discretized directly in physical space. In fact, the entire computation domain (fluid and solid) is divided into a finite number of small control cells and in every cell the integral equations written in discrete form are satisfied. The solution to time t is given in terms of the average cell value of the vector of conservative variables (U). The update of U at the time $t + \Delta T$ from the solution at the time t is obtained by relations based on a discretization of the governing equations (3) that can be written in this compact form

$$\frac{\partial U}{\partial t} = RHS(U) \tag{18}$$

where the calculation of RHS(U) requires the evaluation of the fluxes of the variables conserved on the faces of each cell. An implicit numerical scheme discretizes in time eq.18 as follows:

$$\frac{U^{n+1} - U^n}{\Delta t} = RHS^{n+1} \tag{19}$$

where n denotes the time index. Linearizing RHS^{n+1} eq. 19 becomes

$$\frac{U^{n+1} - U^n}{\Delta t} = RHS^n + \left(\frac{\partial RHS}{\partial U}\right)^n (U^{n+1} - U^n)$$
(20)

The dual time stepping technique is used to obtain the evolution over time of the fluid dynamic and thermal fields. This technique consists in dividing the time steps (Δt) into internal steps $(\Delta \tau)$. The system of equations is then rewritten as follows:

$$\left(\frac{I}{\Delta \tau} + \frac{I}{\Delta t} - \left(\frac{\partial RHS}{\partial U}\right)^*\right) \delta U^* = RHS^* - \frac{U^* - U^n}{\Delta t}$$
 (21)

with $\delta U^* = U^{**} - U^*$, Δt the physical step, $\Delta \tau$ the virtual step, I the matrix identity. At the beginning of the physical step, $U^* = U^n$ is set and U^{**} is iteratively computed from Eq. 21 At this point the physical solution is updated by placing $U^{n+1} = U^{**}$ and advancing Δt . This scheme allows you to use any approximated method to accelerate convergence without reducing temporal accuracy, as these methodologies are applied only to the internal steps which do not affect the final solution [12]. However, if on the one hand dual time stepping simplifies the use of convergence acceleration techniques, on the other hand, it is necessary to find the most convenient combination between the time discretization step Δt and the number of internal steps especially in the integration of a problem that combines the equations of fluid dynamics with the thermal equation of a solid.

4.3 Conjugate heat transfer

Conjugate heat transfer (CHT) simulations rely on a fully integrated method (John et al., 2019). This method employs an identical computational framework, utilizing Equation (14), to concurrently solve the energy equation within solid and fluid regions, albeit with differing formulations for each phase. This strategy enables simultaneous resolution of fluid dynamics and thermal fields within the solid.

5. Domains, boundary conditions and computational meshes

Numerical simulations are performed using Metacomp's CFD++ [12] which has the fully coupled CHT solver. Since we are analyzing solids of revolution, CFD++ offers the opportunity to use an axisymmetric 2D code in order to speed up the calculation procedure. Therefore, computational grids are two-dimensional and composed of triangular cells.

In this work we considered different flight conditions. The propulsive ascent phase, ascent without propulsion, descent with and without retro-propulsion, descent with inflatable ballute. Consequently, different boundary conditions exist and different computational meshes have been used. The grids used in the present study were generated with the Ansa software of BETA CAE Systems [19].

5.1 Ascent and descent phases

5.1.1 Domain

The overall domain is split into two sub-domains, that share the interface between the solid and fluid part. The Figure 4 shows the sub-domain for the fluid-phase in blue and the sub-domain for the solid-phase in red with the respective boundary conditions for the ascent. Meanwhile, the domain of the descent has the same characteristics of the domain in Fig. 4 except for the nose of the rocket, as said in 2.1, and in the boundary conditions. Specifically, the inlet and outlet are reversed for ascent and descent.

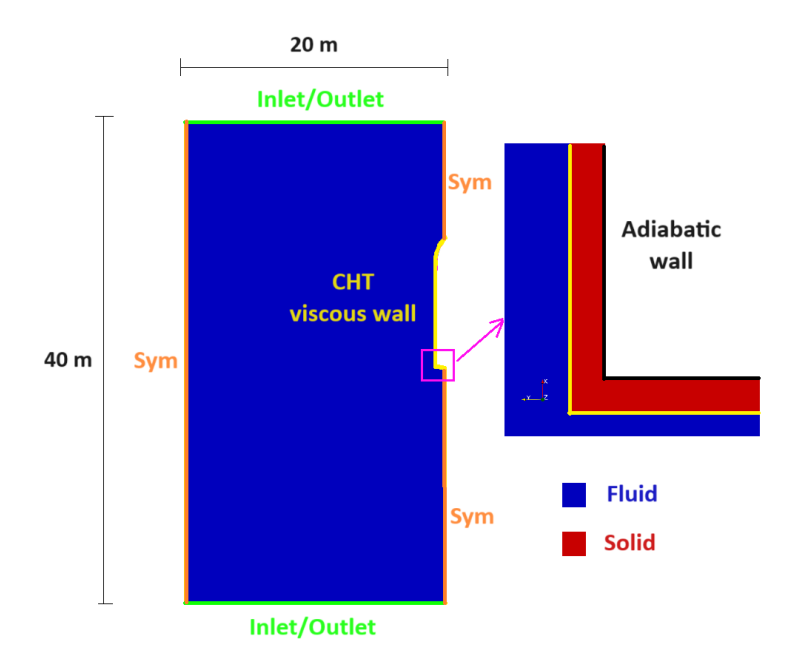


Figure 4 – Overall domain for ascent-phase

	Fluid-	phase	Solid-phase		
Boundaries	prop.	no prop.	prop.	no prop	
Inlet	Variable over time	Variable over time	//	//	
Outlet	Supersonic outlet	Supersonic outlet	//	//	
Symmetry	Symmetry	Symmetry	//	//	
Interface	Conjugate heat	Conjugate heat	Conjugate heat	Conjugate heat	
Fluid-Solid	transfer	transfer	transfer	transfer	
Nozzle	Variable over time	Inviscid wall	//	//	
Solid	//	//	Adiabatic solid wall	Adiabatic solid wall	

Table 4 – Boundary conditions for the ascent in fluid and solid-phases

5.1.2 Boundary conditions

The boundary conditions for the propulsive and non-propulsive phases are summarized in the Tab.4: As mentioned in paragraph 4.3, the simulation is unsteady and in particular the freestream conditions vary with time during the ascent and the descent. For the purpose of simulating the flow, we provide an input file, with the variations of pressure, temperature, the x, y, z components of the velocity, the turbulent viscosity and the concentrations of the gas mixture as a function of time. This is also true at the nozzle exit where we vary the thrust during the ascent phase. In the outlet, however, we impose a supersonic outlet where nothing is prescribed and all values are extrapolated from the interior.

5.1.3 Computational mesh

The computational grids, for the ascent and descent phases are shown in the Figs.5-a and 5-b. They exhibit a wall clustering around the body and in the region of the engine exhaust jet. The characteristics of the grids used for this test case are reported in Tab.5.

Туре	Fluid		5	Solid	Overall		
	N° of points	N° of elements	N° of points	N° of elements	N° of points	N° of elements	
Ascent	18401	36020	5820	10836	24221	46856	
Descent	16613	32496	5282	9841	21895	42337	

Table 5 – Characteristics of the ascent and descent meshes

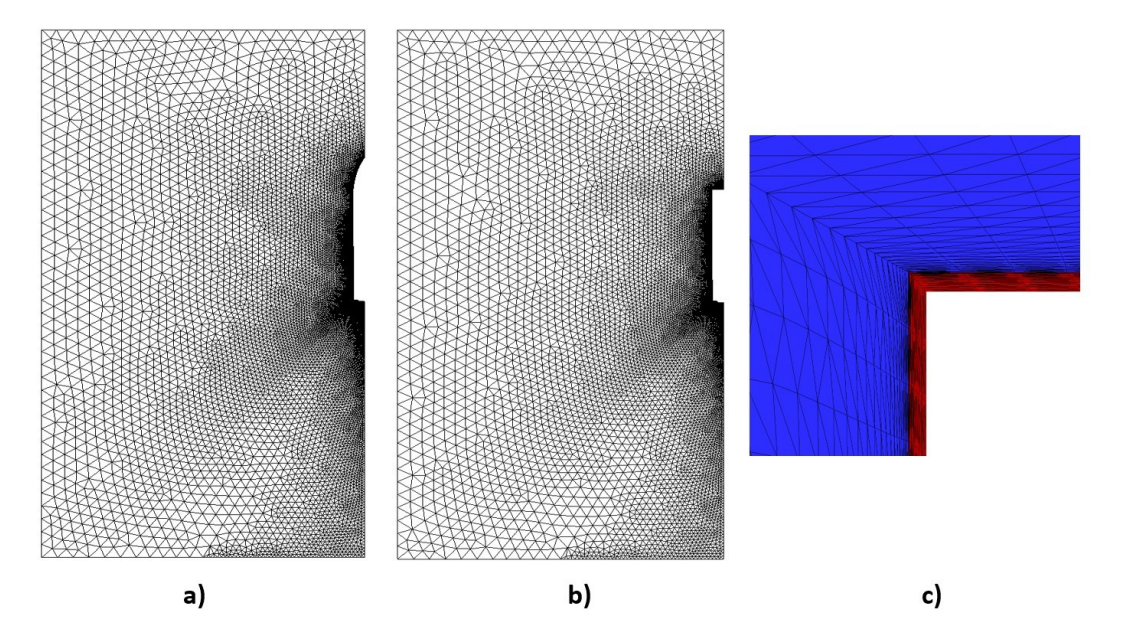


Figure 5 – a) Computational mesh for ascent-phase; b) Computational mesh for descent-phase; c) Computational mesh at the fluid-solid interface

5.2 Descent-phase with inflatable ballute

5.2.1 Domain

The domain used in the presence of the inflatable ballute is shown in Fig. 6. In this case three sub-domains have been considered because the toroid is present together the fluid and the solid phases. The toroid and the solid have distinct characteristics listed in the tables 1 and 3, and different thicknesses, as clearly depicted in the Fig.6. The boundary conditions are the same to those listed in Tab.4 and they also reported in the figure.

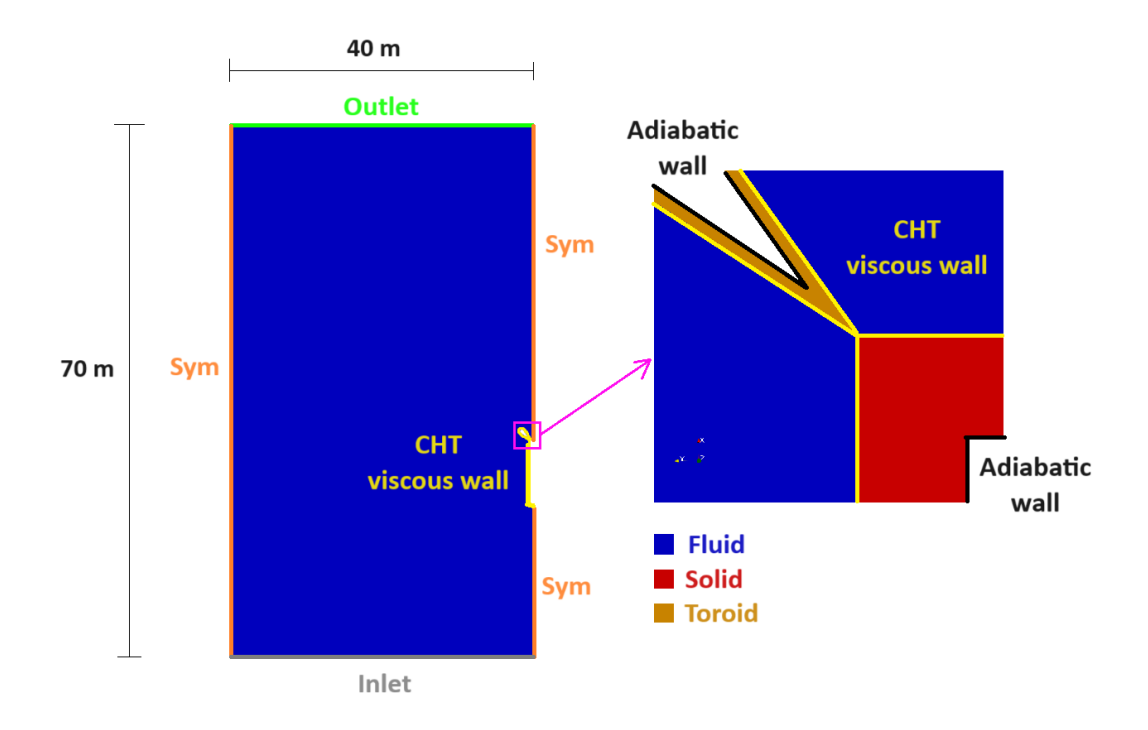


Figure 6 – Overall domain for inflatable ballute

5.2.2 Computational mesh

The computational grid is shown in Fig.7a-7-b. In this case, we only have the descent phase without propulsion, so we are interested in modeling the presence of the shock wave to understand the aerodynamic heating of the different solid parts. For this reason, the grid is clustered near the body and in front of the nozzle exit.

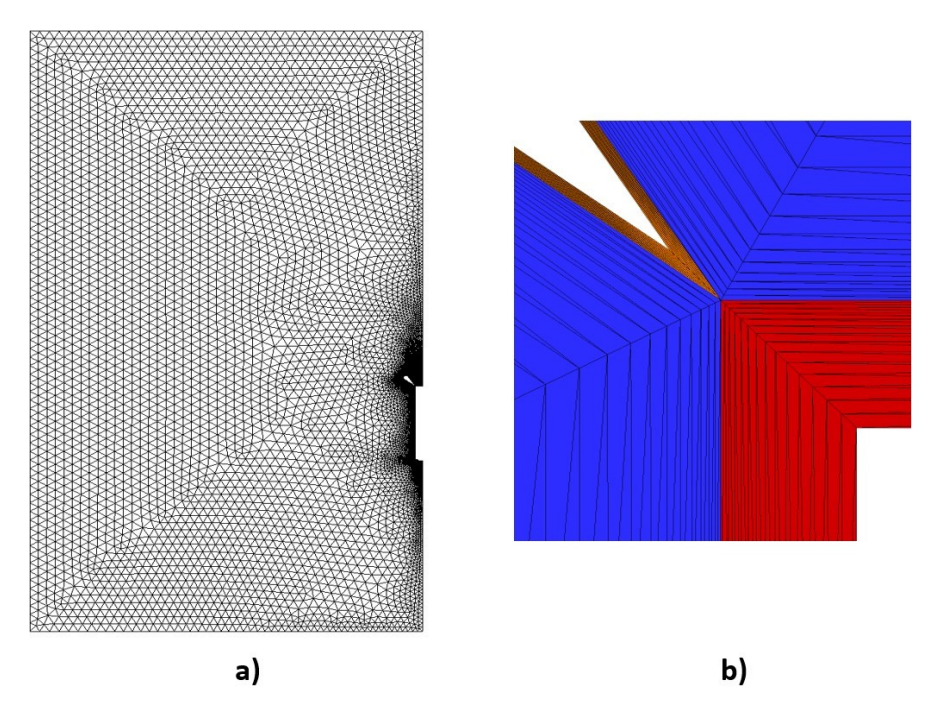


Figure 7 – a) Computational mesh of the inflatable ballute; b) Computational mesh at the interface

The characteristics of the grids used for the inflatable ballute is reported in Tab.6.

F	luid	Solid rocket		Solid	d ballute	Overall		
N° of	N° of	N°of	N° of	N° of	N° of	N° of	N° of	
points	elements	points	elements	points	elements	points	elements	
26169	51177	4920	9156	2463	4223	33552	64556	

Table 6 - Characteristic of the ballute meshes

6. Results

In this paragraph will be presented the results obtained from the CFD simulations for all the different phases described earlier. Specifically, wall heating as well as the variation of aerodynamic drag for the different flight phases will be analyzed. Finally, the comparison between the different trajectories will be presented and the results will be discussed.

6.1 Computation of initial trajectory

An initial trajectory of the rocket is used to determine the variations of the variables over time to provide as input file in CFD++. Two C_D constant values are chosen for the ascent and the descent trajectory respectively of 0.75 and 1.5. The first is the typical value of a rocket during its ascent phase [20] while the second is the typical value for a similar sized flat plate. The initial trajectory is obtained by integrating equations (1) through the fourth-order Runge-Kutta method explained in section 4.1. The following initial and integration conditions are reported:

- $r_0 = 0.01 \ km$
- $\theta_0 = 89.5 \ deg$

- $V_0 = 0.745 \ m/s$
- $t_0 = 2.6 \ s$
- $\Delta t = 0.2$

where r_0 is the initial altitude of the rocket, θ_0 is the initial flight path angle, V_0 is the initial velocity, t_0 is the initial time and Δt is the step size for the integration. The freestream conditions vary with the altitude and they are computed using Earth-GRAM [17]. For the nozzle exit, an initial thrust of 100% was assumed, but after 60.4 seconds, the thrust is reduced to 75%, and finally, engine is stopped after 120.6 seconds. For the descent part no retro-propulsion and 10 seconds retro-propulsion are considered. Figure 8 shows the trajectories in terms of Mach and time.

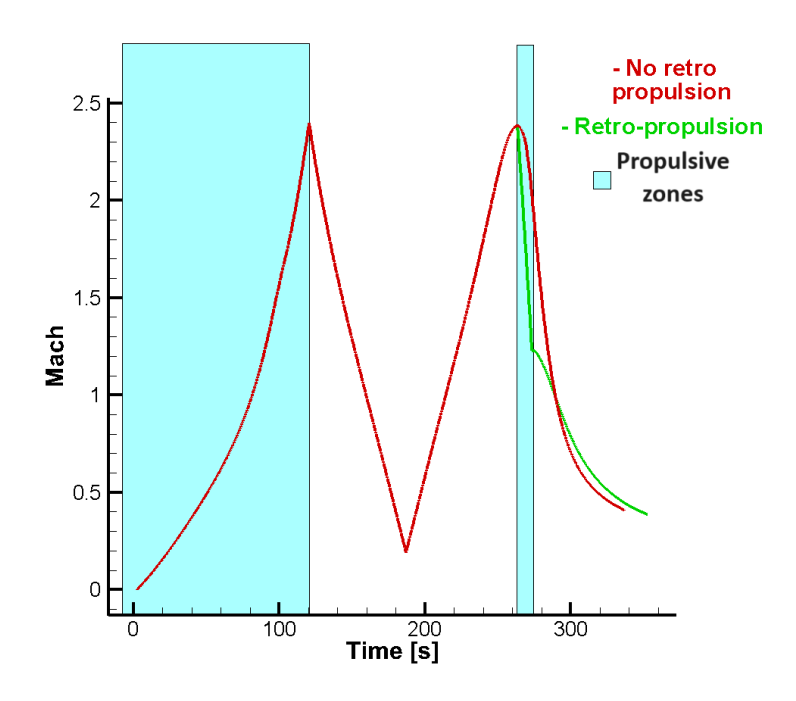


Figure 8 - Initial trajectory

6.1.1 Ascent

As specified in section 5.1.2 a time variable flow is provide at the inlet and nozzle exit. The time variable conditions for the inlet are taken from the initial trajectory and they are listed in the Tab.7, while for the exit nozzle these conditions are shown in Tab.8. CFD++ requires n-1 gas concentrations as input and the last one is computed by CFD++ itself, so we provide three gas concentrations, Air, CO and CO_2 , while H_2O is computed automatically by CFD++.

Time	P_{∞}	T_{∞}	u	٧	W	$ ilde{\mathcal{V}}_t$	Air	CO	CO_2
S	Pa	K	m/s	m/s	m/s				
14.0	98840	300	-34.82	0.0	0.0	1.6e-6	1.0	0.0	0.0
60.4	44460	257.8	-283.91	0.0	0.0	2.7e-6	1.0	0.0	0.0
121.0	671.3	242	-715.94	0.0	0.0	1.6e-4	1.0	0.0	0.0
188.0	24	244.7	-59.35	0.0	0.0	4.6e-3	1.0	0.0	0.0

Table 7 – Inflow profile for the inlet

To perform the CHT simulation, an initial material temperature has been set at 300 K. Additionally, it is worth noting that we are conducting an unsteady simulation using a numerical integration based on dual time-stepping, as explained in section 4.2. For this test case, a global time-step dt of 0.01s is divide into 20 internal iterations.

Time	P_{∞}	T_{∞}	u	٧	W	$ ilde{ ilde{ u}}_t$	Air	CO	CO_2
S	Pa	K	m/s	m/s	m/s				
14.0	55204	1578.17	-2922.8	0.0	0.0	1.84e-09	0.0	0.23386	0.25598
60.4	41204	1552.06	-2910.5	0.0	0.0	1.65e-09	0.0	0.23580	0.25296

Table 8 – Inflow profile for the exit nozzle

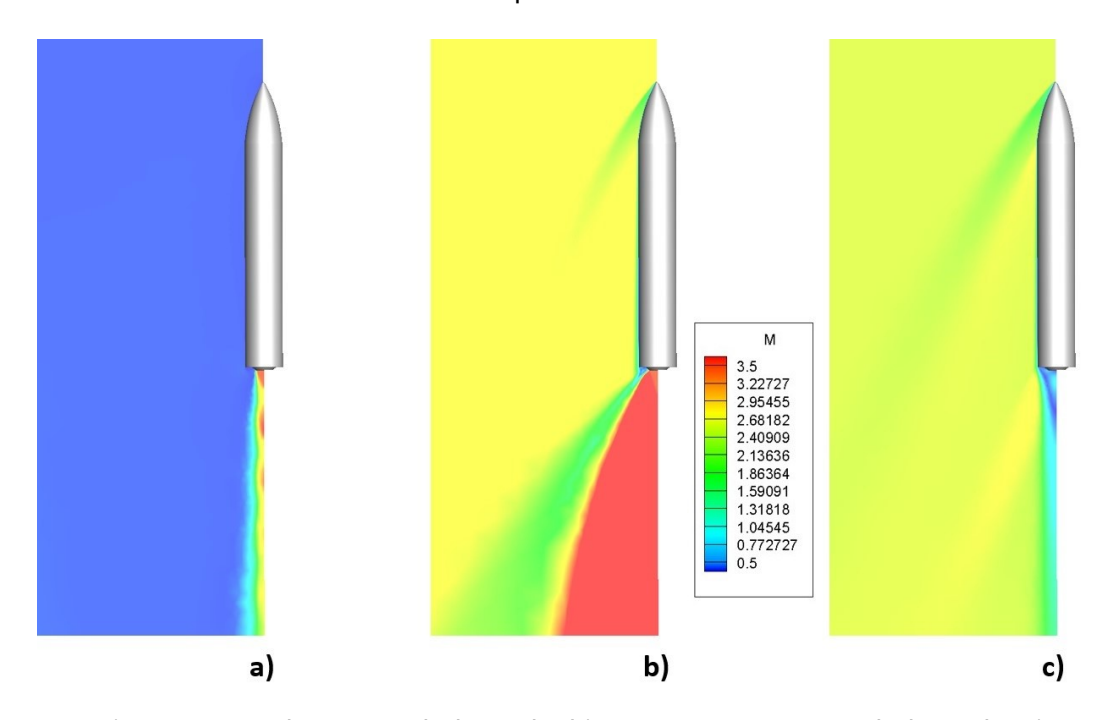


Figure 9 – a) t = 15 s, underexapanded nozzle; b) t = 120 s, overexpanded nozzle; c) t = 135 s, ascent without propulsion

The Mach field is shown in the Figs.9. Figures 9.a and 9.b show the Mach number field in two different time instants where the propulsion is active. Figure 9.c shows the Mach field in a time where the engine is turned off. It can be observed that Fig. 9.a show a subsonic field with an overexpanded nozzle exit, as the pressure at the nozzle exit is lower than the freestream pressure. Conversely, Fig. 9.b shows a supersonic field with an underexpanded jet.

The Fig.10 plots the temperature variation over time in three different points on the rocket wall to assess heating due to the presence of the propulsive flow and the external flow. The blue line represents the behavior in the corner between the base of the rocket and the body and shows a heating of about 20 K mainly caused by the presence of the propulsive jet. The orange line represents the temperature history in the point at the middle of the body and shows a decrease of the temperature of about 4 K. Finally, the pink line shows the variation in the nose of the rocket and after a heating of some Kelvin the wall cools. This apparently strange behavior of the last two points can be explained through the decrease of the ambient temperature that take place as the altitude increase. Overall, the temperature of the side wall remains approximately unchanged.

The Fig.11 represents the variation of the drag coefficient, C_D , w.r.t. the time in the ascent-phase, computed using the equation 2. During the propulsive phase, depicted by the red line, the C_D is lower compared to the no-propulsive ascent represented by the blue line. This occurs because the presence of propulsion, especially in the underexpanded flow condition, results in less expansion of the flow at the corner region and consequently, higher pressure on the base, which reduces aerodynamic drag during the ascent phase.

6.1.2 Descent

To calculate the descent phase, the thermal state obtained at the end of the ascent phase is used as initial thermal state. The inlet and outlet in the domain are now inverted, as explained in Section 5.1.1.

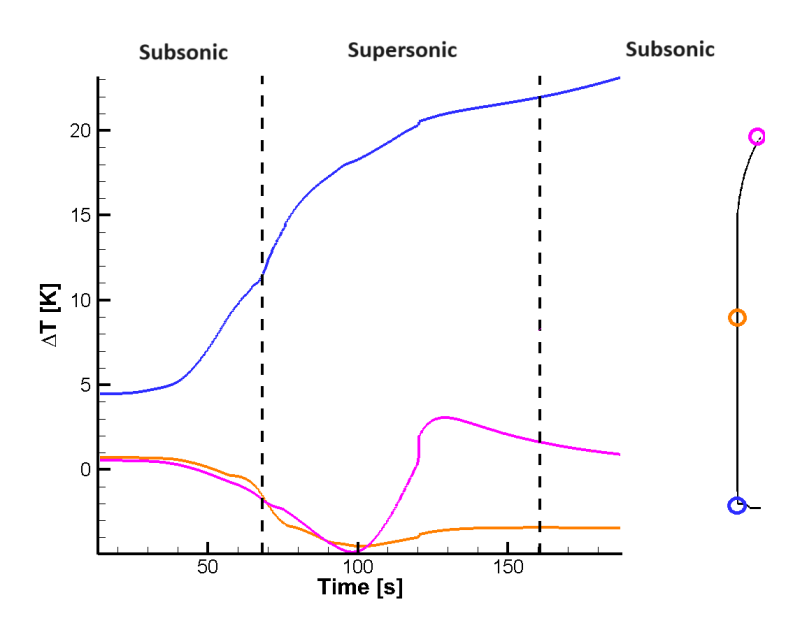


Figure 10 – Variations of the temperature w.r.t time in the ascent-phase

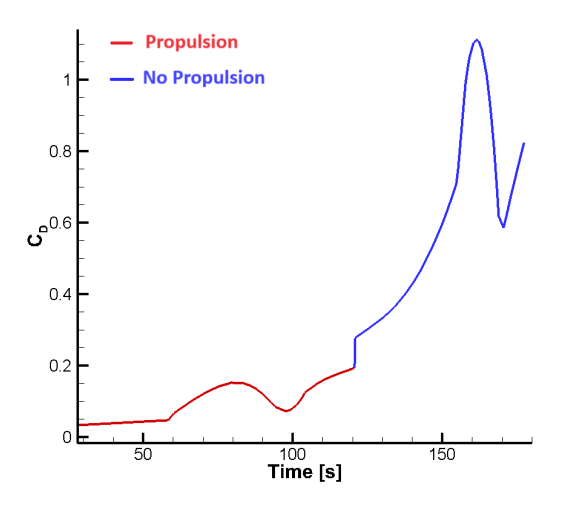


Figure 11 – Variations of the C_D w.r.t time in the ascent-phase

For the descent phase, two different scenarios were considered: descent without retro-propulsion, in order to investigate only the effect of the aerodynamic heating and with 20 seconds of retro-propulsion at 100% of thrust. The external flow conditions of the two scenarios are outlined in the tables 9-10. The table 9 displays data for descent without propulsion, whereas the table 10 presents data for retro-propulsion.

Time	P_{∞}	T_{∞}	u	٧	W	$ ilde{\mathcal{V}}_t$	Air	CO	CO_2
S	Pa	K	m/s	m/s	m/s				
200	26.05	246.2	182.08	0.0	0.0	4.3e-3	1.0	0.0	0.0
259	958.4	234.9	750.07	0.0	0.0	1.1e-4	1.0	0.0	0.0
269	3129.0	215.3	818.47	0.0	0.0	3.0e-5	1.0	0.0	0.0
279	7221.0	197.4	822.56	0.0	0.0	1.0e-5	1.0	0.0	0.0

Table 9 – Inflow profile for the inlet without retro-propulsion

Figures 12 shows the temperature fields during descent at three different times where the external

Time	P_{∞}	T_{∞}	u	٧	W	$ ilde{\mathcal{V}}_t$	Air	CO	CO_2
S	Pa	K	m/s	m/s	m/s				
200	26.05	246.2	182.08	0.0	0.0	4.3e-3	1.0	0.0	0.0
259	958.4	234.9	750.07	0.0	0.0	1.1e-4	1.0	0.0	0.0
269	2514.0	218.6	531.81	0.0	0.0	6.1e-5	1.0	0.0	0.0
279	4774.0	206.9	272.50	0.0	0.0	2.45e-5	1.0	0.0	0.0

Table 10 – Inflow profile for the retro-Propulsion

flow is subsonic (Fig.12.a) and supersonic (Figs.12.b and 12.c). Figure 12.c shows also the temperature field when the retro-propulsion is active. We can immediately observe the temperature differences in these three phases: in the subsonic case, the maximum temperature is about 300 K, therefore, in this phase, the material around the base of the rocket cools. In the supersonic case,

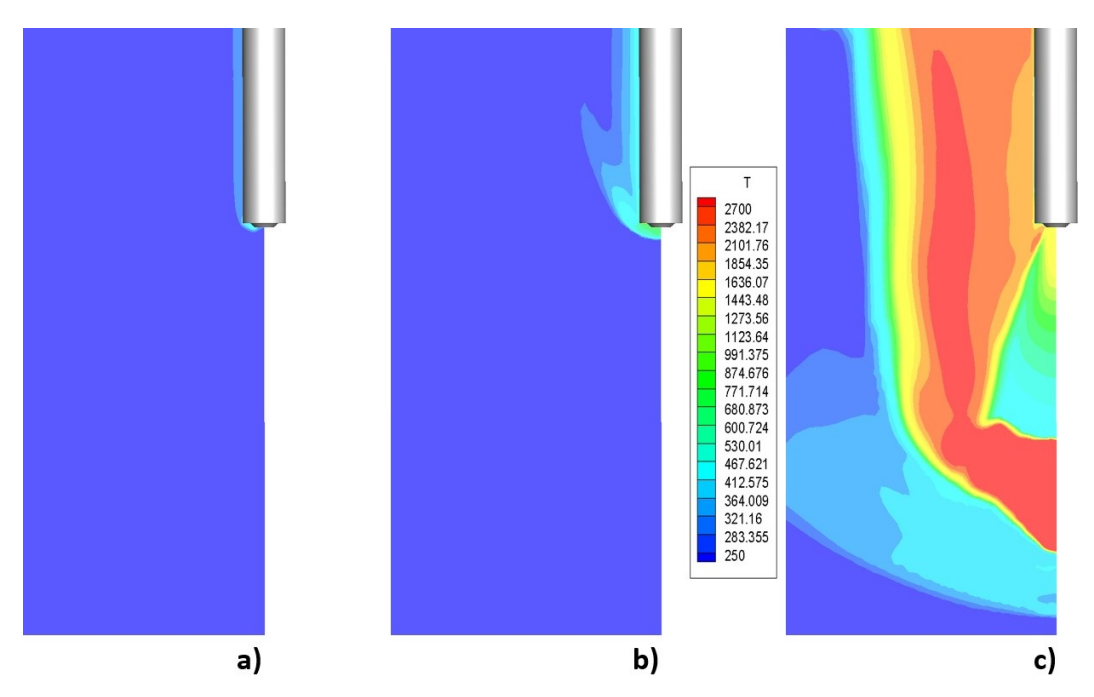


Figure 12 - a) Temperature field at t = 188 s; b) Temperature field at t = 259; c) Temperature field at t = 269 s for retro-propulsion

without the retro-propulsion the temperature reaches about 400 K, therefore, after a certain time the material will begin to heat up. In the retro-propulsion phase, the hot jet exiting from the nozzle is deflected by the external stream and return back touching the side wall with temperatures of about 2000 K, much higher than the previous two conditions.

The Fig.13 shows in details the variation of the temperature w.r.t. the initial value of 300 K, in the case of descent without retro-propulsion. The blue line represents the temperature behavior at the corner at the rocket's base. The temperature continues to increase during the descent phase, especially in supersonic regime, where the effect of the shock wave causes a heating of about 60 K in this point. The orange line represents the point at the middle of the rocket. The variation of temperature w.r.t. the initial temperature is always negative, but due to the aerodynamic effects, the temperature increase with a $\Delta T = 1K$ after 270 seconds.

The Fig.14 shows the variations of temperature w.r.t. the same two points. In this case the retropropulsion is activated for 20 seconds. Compared to the previous case, the blue line reaches about the same temperature. So, the aerodynamic heating and the heating due to the propulsion cause the same effect. This means that, at the base of the rocket the effects of aerodynamic heating must be evaluated for faster flow because they could be very important. Indeed, in the middle of the rocket (the orange line) the temperature grows linearly up to about $\Delta T = 12K$. Thus, the presence of propulsion significantly increases the temperature on the side region of launcher.

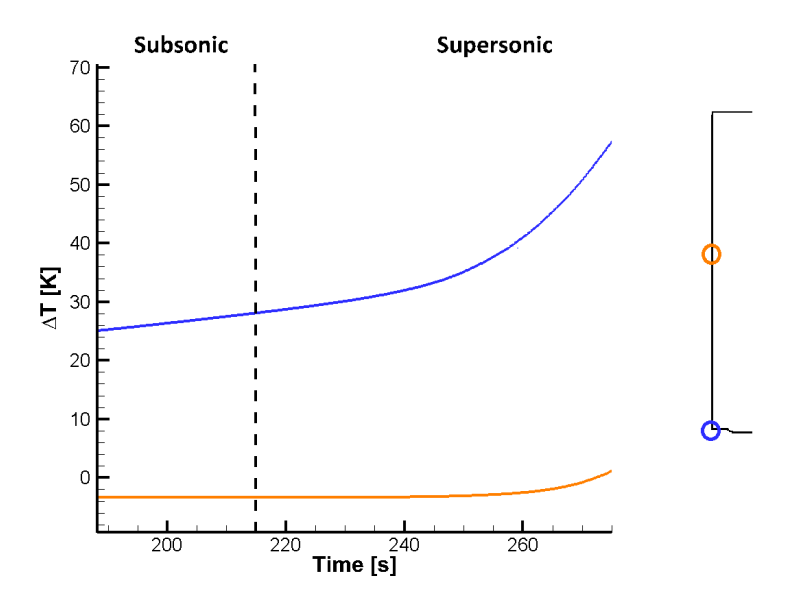


Figure 13 – Variations of the temperature w.r.t time in the descent-phase without retro-propulsion

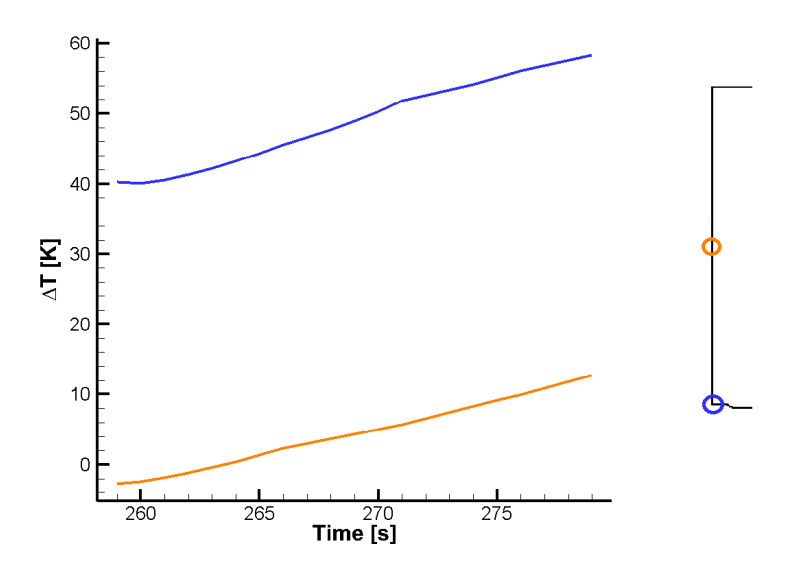


Figure 14 – Variations of the temperature w.r.t time in the descent-phase with retro-propulsion

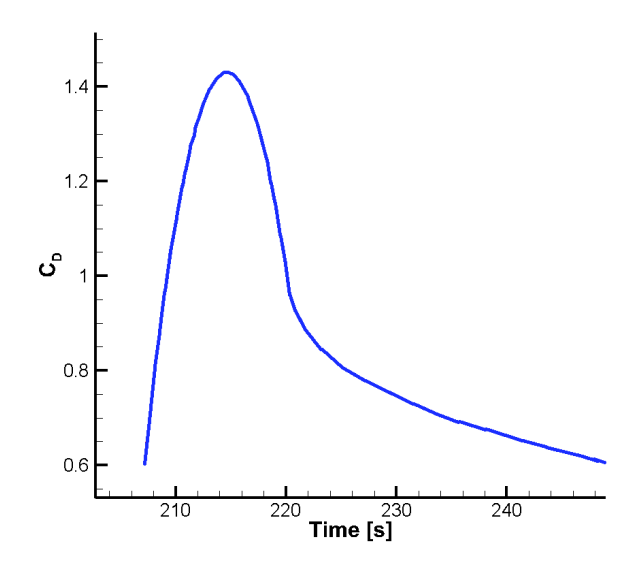
The Fig.15 and the Fig.16 show the variation of the drag coefficient w.r.t. time for the descent phase with and without retro-propulsion.

The Fig.15 represents the descent-phase without retro-propulsion in which only the aerodynamic forces decelerate the rocket. C_D starts with a low values in a subsonic field and then increases reaching the maximum in the transonic regime, as expected. Then, in the supersonic field its value decreases until $C_D=0.6$

The propulsion decreases the C_D value also in the case. Indeed, the Fig.16 shows a sharp decrease of C_D caused by the presence of the jet at the nozzle exit that, in the supersonic field, "pushes" the shock wave away from the rocket, reducing the pressure at the wall and, consequently, significantly decreasing the value of the C_D .

6.1.3 Descent with inflatable ballute

The simulation begins directly from the descent phase with an initial temperature set to 300 K for the rocket and the ballute. The values of the time step dt and the internal iterations of the dual time-step



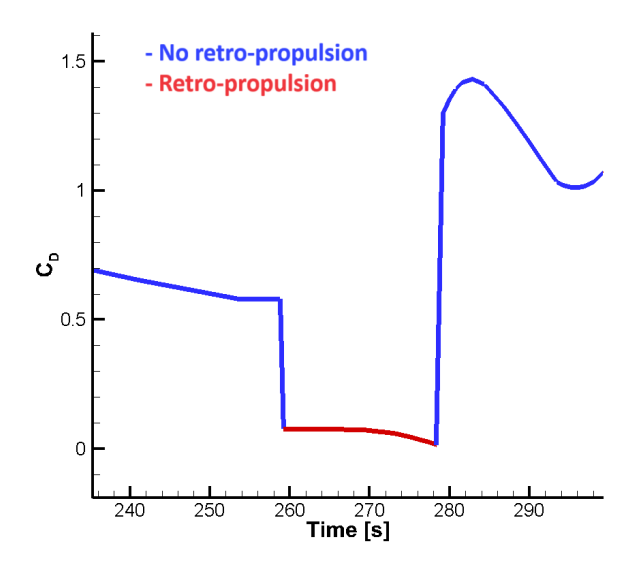


Figure 15 – Variations of the C_D w.r.t time in the descent-phase without retro-propulsion

Figure 16 – Variations of the C_D w.r.t time in the descent-phase with retro-propulsion

are the same as in the previous case. In the table 11, the time variable conditions are reported.

Time	P_{∞}	T_{∞}	u	٧	W	$ ilde{ u}_t$	Air	CO	CO_2
S	Pa	K	m/s	m/s	m/s				
200	35.48	253.3	233.86	0.0	0.0	3.2e-3	1.0	0.0	0.0
235	264.19	268	547.69	0.0	0.0	8.1e-4	1.0	0.0	0.0
267.4	2625.0	218.0	443.15	0.0	0.0	4.3e-5	1.0	0.0	0.0

Table 11 – Inflow profile for the inlet inflatable ballute

The figures 17 present a comparison in terms of temperature field at different time instants for the ballute. The Fig.17.a shows the temperature field in a subsonic field, while the Figs.17.b and 17.c represent the supersonic field.

Figure 18 shows in details the variation of the temperature over time in four different points of the ballute. Specifically, the inflatable ballute cools down under these conditions, as demonstrated by a negative variation of temperature ΔT , but in the supersonic phase, they tend to heat up due to the presence of the shock wave. Even if it remains below to the structural limits of the chosen material, this suggests that for higher Mach numbers and a longer exposure time to the supersonic flow, temperatures may be higher. The red line of Fig.18 represents the point at the interface between the rocket and the inflatable ballute and its temperature remain almost constant during the descent. The blue line represents the point that has the maximum value of temperature of the ballute of about 289 K and the point where the temperature increases fastest.

The gray line represents a point in the back of the structure and its temperature is lower w.r.t. the other points because it experiences an expansion of the fluid and, so, a lower value of the temperature. Figure 19 shows the variation of the C_D product with respect to time, that present the higher values due to the presence of the inflatable ballute.

6.2 Trajectories

Three different conditions were chosen: trajectory for descent without retro-propulsion; 10 seconds of retro-propulsion and descent with inflatable ballute.

The first two figures 20 and 21, show the comparison between the trajectory computed using the constant C_D and the trajectory recomputed using the variable C_D obtained by the CFD simulations. In

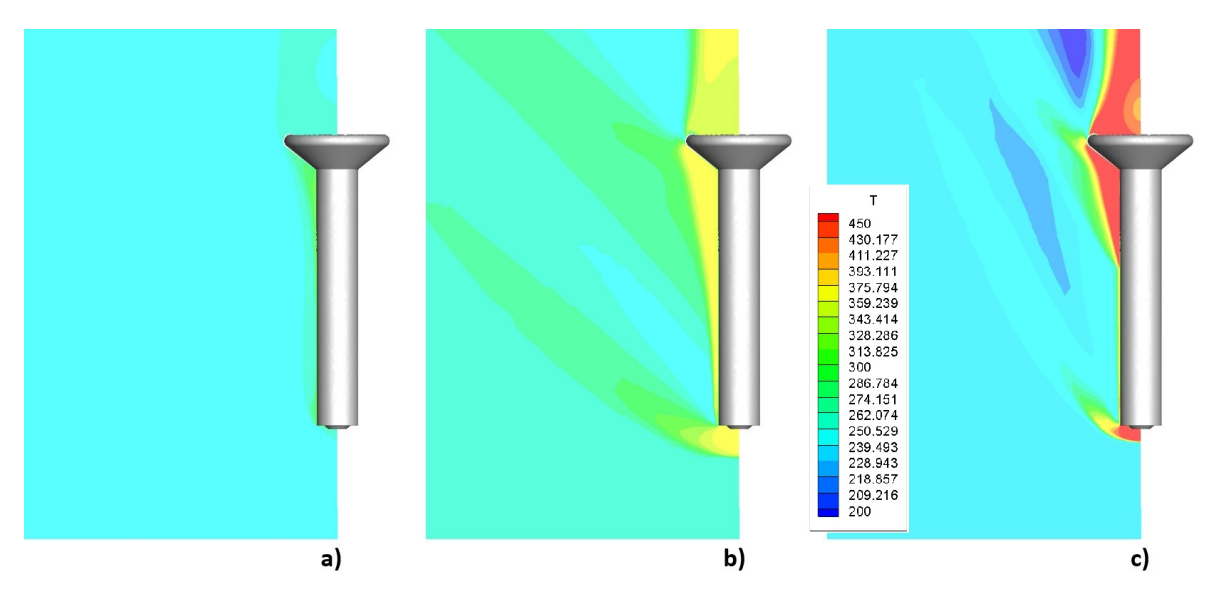


Figure 17 – a) Temperature field at t = 200 s; b) Temperature field at t = 239; c) Temperature field at t = 267 s

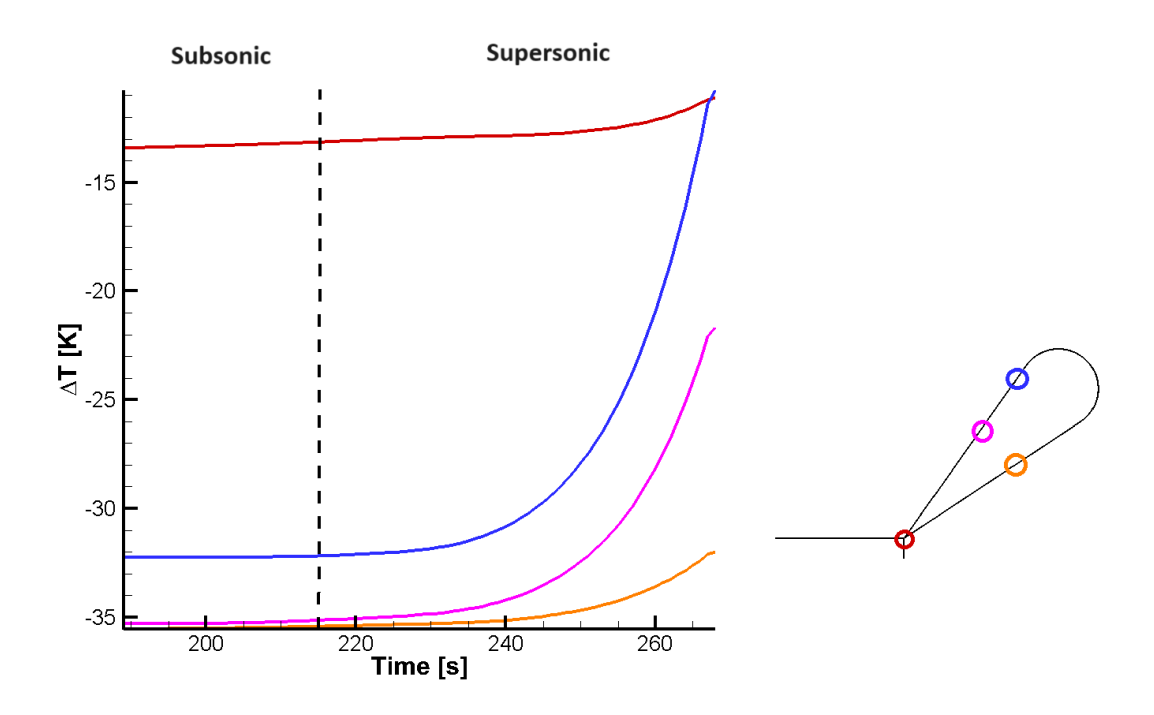


Figure 18 – Variations of the Temperature w.r.t time in the descent with ballute

Fig.20 the retro-propulsion in not used while in Fig.21 is used.

In both cases, in the ascent phase the maximum difference is about for M=1 but at the end of the ascent, the two trajectories remain approximately the same because thrust has a more significant impact on the trajectory w.r.t. the aerodynamic forces. Indeed, the main differences occur during the descent, where only the aerodynamic forces are present and the retro-propulsion lasts for few seconds. For this reason, variations in the drag coefficient cause substantial deviations in the trajectory and the rocket reaches a higher speed w.r.t. the case where C_D is assumed constant. In particular, the final velocity of the trajectory recomputed using the C_D obtained from CFD simulations (the blue line of Fig.20), is M=0.69 while the red trajectory computed using the constant C_D shows a final velocity of M=0.4. The same consideration can be done for the retro-propulsion. In particular, the blu line of Fig.21 shows that in the retro-propulsion trajectory estimated using the C_D obtained by CFD, the velocity are greater than ones estimated by using constant C_D values. So, due to the lower

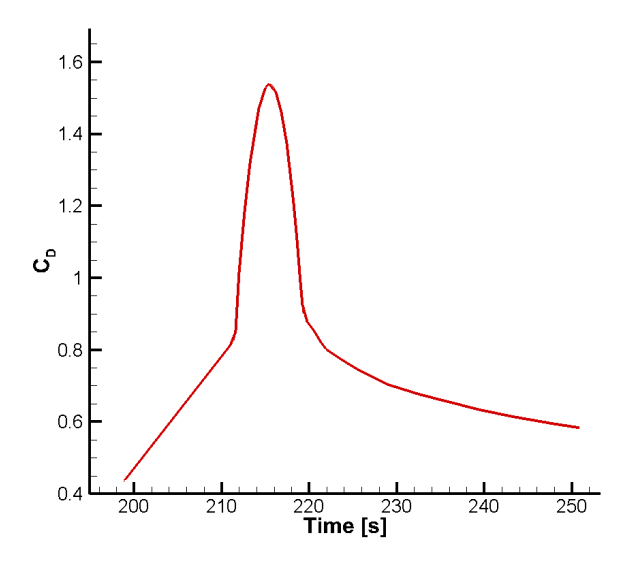
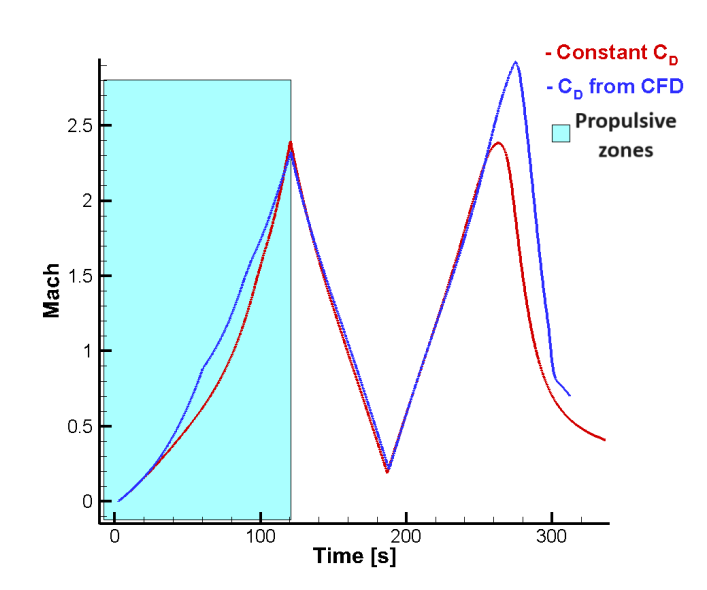


Figure 19 – Variations of the C_DA w.r.t time in the descent with ballute

C_D values, the rocket tends to re-accelerate after the propulsive braking for a short time.



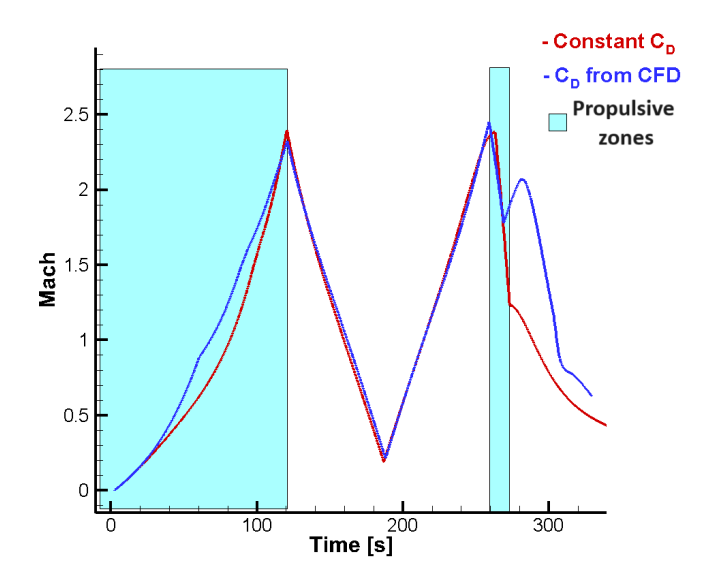


Figure 20 – Comparison between initial and final trajectory without retro-propulsion

Figure 21 – Comparison between initial and final trajectory with retro-propulsion

To compute the mass savings due to the use of the inflatable ballute, it is necessary to consider a different initial mass of the rocket which takes into account the exclusion of the mass due to the retro-propulsion and the inclusion of the mass due to the inflatable. Consequently, the initial mass of the system is lower than that used for the previous cases. Tab.12 shows the mass comparison between the rocket with retro-propulsion and with the inflatable ballute. In particular, the initial mass for the last is computed by subtracting the mass consumed during retro-propulsion (276 kg) and adding the mass of the inflatable (56.75 kg). It is evident that it is necessary reduce the propulsive phase to obtain the same ascent trajectory as the figures 20-21 and, consequently, the mass consumed by the propulsion is lower than the rocket. Therefore, the mass saving is 473.25 kg.

Figure 22 compares the three trajectories with or without the use of retro-thrusters and the use of the inflatable ballute. The trajectory obtained in the case of the inflatable is represented by the green

	Initial	Ascent mass fuel					
	mass	consumption					
Rocket with retro-propulsion	6000 kg	3257 kg					
Rocket with ballute	5780.75 kg	3003 kg					
Mass saving 219.25 kg 254 kg							
Overall Mass saving: 473.25 kg							

Table 12 - Mass saving

line. In this case the rocket decelerates the more, reaching the ground with a speed equal to M = 0.36 w.r.t. the retro-propulsion case in which M = 0.62 is reached. Consequently, the advantages in the use of the inflatable ballute in terms of speed and mass saving are evident.

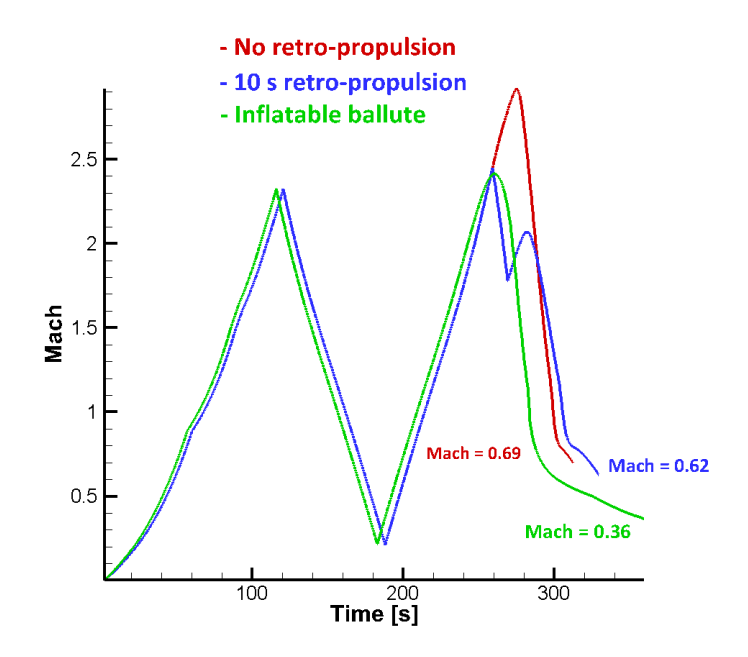


Figure 22 – Comparison between the trajectories without and retro-propulsion and of the inflatable ballute

6.3 Considerations

The advantages in using inflatable ballutes are evident. Indeed, it is possible to reduce much speed during the descent phase compared to the case where retro-propulsion is used. Furthermore, this allows significant mass savings as no propellant is consumed during the descent phase, and in addition this mass can be eliminated from the rocket which will be further lighter.

Compared to the use of retro-propulsion, the advantages in terms of heating are not so important in the analyzed cases. In fact, at the base of the rocket we have about the same heating of the wall caused by the supersonic flow and by the retro-propulsion. Nevertheless, this test-case analyzed in the present work considers relatively low Mach number flows whose maximum is around 2.5. In higher speeds re-entries the effect of aerodynamic heating and of the retro-propulsion could more important. Therefore, more detailed analysis are necessary.

A disadvantage in using the inflatable ballute adopted in our study is the lack of aerodynamic control as can instead occur through fin grids which can direct the landing of the first stages in specific areas. Therefore, it will be necessary to investigate new solutions that allow aerodynamic trajectory control.

7. Conclusions

Preliminary results on the use of inflatable ballutes to decelerate the first stage of a launcher during its reentry phase have been presented in this paper. In detail, these devices were installed on a

simplified single-stage launcher considered in our benchmark. 2D axis-symmetric computations of both the launcher ascent and the descent flight phases were performed using the commercial gas-dynamic solver CFD++. Due to the presence of the propulsive jet, the heating on the base and around the body is generally smaller than the limit threshold of the material. The computed trajectories suggest great advantages in using these inflatable devices which allow us to reduce landing speed and maintain relatively low wall temperatures. Finally, tests at higher Mach values will be carried out, in future work, to evaluate the effects of aerodynamic heating and retro-propulsion to evaluate the aerodynamic heating which could significantly increase the wall temperature more than the retro-propulsion.

8. Contact Author Email Address

valerio.orlandini@uniroma1.it renato.paciorri@uniroma1.it alessia.assonitis@uniroma1.it aldo.bonfiglioli@unibas.it

9. Copyright Statement

The authors confirm that they, and/or their company or organization, hold copyright on all of the original material included in this paper. The authors also confirm that they have obtained permission, from the copyright holder of any third party material included in this paper, to publish it as part of their paper. The authors confirm that they give permission, or have obtained permission from the copyright holder of this paper, for the publication and distribution of this paper as part of the ICAS proceedings or as individual off-prints from the proceedings.

References

- [1] Irwin I Shapiro and Harrison M Jones. Perturbations of the orbit of the echo balloon. *Science*, 132(3438):1484–1486, 1960.
- [2] David Cadogan and John Lin. Inflatable solar array technology. In *37th Aerospace Sciences Meeting and Exhibit*, page 1075, 1999.
- [3] Aman Chandra, Juan Carlos Lopez Tonazzi, Douglas Stetson, Terrance Pat, and Christopher K Walker. Inflatable membrane antennas for small satellites. In *2020 IEEE Aerospace Conference*, pages 1–8. IEEE, 2020.
- [4] D Cadogan, C Sandy, and M Grahne. Development and evaluation of the mars pathfinder inflatable airbag landing system. *Acta Astronautica*, 50(10):633–640, 2002.
- [5] Nathan D Wells and Eric I Madaras. The potential for health monitoring in expandable space modules: The bigelow expandable activity module on the iss. In *International Workshop on Structural Health Monitoring (IWSHM 2017)*, number JSC-CN-39605, 2017.
- [6] John DiNonno and Neil Cheatwood. Low-earth orbit flight test of an inflatable decelerator (loftid) mission overview and science return. In *AIAA SCITECH 2024 Forum*, page 1309, 2024.
- [7] Valerio Orlandini, Renato Paciorri, Alessia Assonitis, Francesco Saltari, and Aldo Bonfiglioli. A fluid dynamics technique for modelling inflatable shield for re-entry or aerocapture missions. In *AIAA AVIATION 2023 Forum*, page 4425, 2023.
- [8] DE Koelle and H Kuczera. Sänger ii, an advanced launcher system for europe. *Acta Astronautica*, 19(1):63–72, 1989.
- [9] Sylvain Guédron, Christophe Bonnal, and Jean Marc Astorg. In-flight experimentation: Guidelines for future lanchers. In 55th International Astronautical Congress of the International Astronautical Federation, the International Academy of Astronautics, and the International Institute of Space Law, pages V–8, 2004.
- [10] P Baiocco and Ch Bonnal. Technology demonstration for reusable launchers. *Acta Astronautica*, 120:43–58, 2016.
- [11] SpaceX. Falcon User's Guide, 2021.
- [12] Sukumar Chakravarthy, Oshin Peroomian, Uriel Goldberg, and Sampath Palaniswamy. The cfd++ computational fluid dynamics software suite. In *AIAA and SAE, 1998 World Aviation Conference*, page 5564, 1998.
- [13] Bibin John, P Senthilkumar, and Sreeja Sadasivan. Applied and theoretical aspects of conjugate heat transfer analysis: A review. *Archives of Computational Methods in Engineering*, 26:475–489, 2019.

- [14] Avio. Sito Web Avio M10, n.d.
- [15] Bonnie J McBride. *Computer program for calculation of complex chemical equilibrium compositions and applications*, volume 2. NASA Lewis Research Center, 1996.
- [16] Matweb. Sito Web Matweb, n.d.
- [17] PW White and J Hoffman. Earth global reference atmospheric model (earth-gram): User guide. Technical report, 2023.
- [18] Philippe Spalart and Steven Allmaras. A one-equation turbulence model for aerodynamic flows. In *30th aerospace sciences meeting and exhibit*, page 439, 1992.
- [19] BETA CAE systems. Ansa home page. https://www.beta-cae.com/ansa.html.
- [20] NASA Glenn Research Center. Model rocket center of gravity and center of pressure. https://www.grc.nasa.gov/www/k-12/VirtualAero/BottleRocket/airplane/rktcodn.html, 2024. Accessed: 2024-06-08.